Reactive power control in photovoltaic systems through (explainable) artificial intelligence

Christian Utama [a,b,*], Christian Meske [c], Johannes Schneider [d], Carolin Ulbrich [b]

[a] Department of Information Systems, Freie Universität Berlin, Germany
[b] PVcomB, Helmholtz-Zentrum Berlin, Germany
[c] Faculties of Mechanical Engineering and Computer Science, Ruhr-Universität Bochum, Germany
[d] Institute of Information Systems, University of Liechtenstein, Liechtenstein

ARTICLE INFO

ABSTRACT

Across the world, efforts to support the energy transition and halt climate change have resulted in significant growth of the number of renewable distributed generators (DGs) installed over the last decade, among which photovoltaic (PV) systems are the fastest growing technology. However, high PV penetration in the electricity grid is known to lead to numerous operational problems such as voltage fluctuations and line congestions, which could be eased by utilizing the reactive power capability of PV systems. To this end, we propose to use artificial neural network (ANN) to predict optimal reactive power dispatch in PV systems by learning approximate input–output mappings from AC optimal power flow (ACOPF) solutions in either a centralized or a decentralized manner. In the case of decentralized control, we leverage Shapley Additive Explanations (SHAP), an explainable artificial intelligence (XAI) technique, to identify non-local grid state measurements which significantly influence the optimal dispatch of each individual system. Both centralized and decentralized ANN-based controllers are evaluated through a case study based on the CIGRE medium-voltage distribution grid and compared to baseline control strategies. Results show that both ANN-based controllers exhibit superior performance, hindering voltage problems and line congestions which are encountered with baseline strategies while recording an energy saving of 0.44% compared to fixed power factor control. By leveraging ANN and SHAP, the proposed decentralized controllers for reactive power control are able to achieve ACOPF-level performance while promoting data privacy and reducing computational burden.

1. Introduction

In accordance with the goal of limiting global warming to well below 2 °C set in the Paris Agreement, concerted efforts have been made all around the world to reduce greenhouse gas emissions from every sector. In the electricity sector, these efforts have manifested in the continuously increasing deployment of renewable distributed generators (DGs) such as photovoltaic (PV) systems and wind turbines alongside the development of strategies to plan future electricity systems with high renewables penetration [1,2]. In Germany, the share of renewables in the gross electricity consumption has grown from 17.1% in 2010 to 45.2% in 2020 [3] and is targeted to continue to grow to 65% by 2030. To achieve this target, the installed capacities of solar and wind energies are projected to increase from 53.1 and 62.2 GW to 100 and 91 GW [4], respectively, making them central to the energy transition. Since electricity production from solar and wind energies relies on intermittent energy sources, i.e., the energy produced at each instant depends on the available solar irradiation or wind speed,

electricity grid operators are required to adapt their operation strategies to cope with the change in the electricity mix.

Traditionally, electricity flows only in one direction, i.e., from large generators connected at the extra high voltage transmission level (> 220 kV) to distribution feeders and end consumers connected at the high (60–220 kV), medium (6–60 kV) and low (230 and 400 V) voltage levels. In this conventional setup, grid operators determine the optimal generation levels of the generators to minimize supply cost while considering load fluctuations and ensuring a reliable and secure electricity supply. In an electricity grid with significant renewables penetration, however, grid operators have to additionally cope with the intermittent and volatile nature of the energy produced by DGs connected at high and medium voltage levels, hence increasing the complexity of the economic dispatch problem. Furthermore, since wind and solar power plants are often sized larger than their conventional counterparts to handle the same load level, reverse power flows from lower to higher

* Corresponding author at: Department of Information Systems, Freie Universität Berlin, Germany.
E-mail address: christian.utama@fu-berlin.de (C. Utama).

Nomenclature

Sets and indices

i	Node/bus
s	Slack node/bus
(ij)	Transmission line connecting node i to j
$h \in H$	Hidden layer in ANN
$k \in K$	Training sample
$m \in M$	SHAP coalition
$t \in T$	Time step
$x \in X$	ANN input feature
$y \in Y$	ANN output
N	Set of nodes/buses
L	Set of transmission lines
G	Set of controllable generators
P_y	Set of important features for output y

Variables and parameters

p_i^g	Active power generation at node i [MW]
q_i^g	Reactive power generation at node i [MVAR]
s_i^g	Apparent power generation at node i [MVA]
$p_i^{g,peak}$	Peak active power generation at node i [MW]
$p_i^{g,current}$	Current active power generation at node i [MW]
p_i^d	Active load at node i [MW]
q_i^d	Reactive load at node i [MVAR]
$p_i^{d,nom}$	Nominal active load at node i [MW]
p_{ij}^f	Active power flowing on transmission line (ij) [MW]
q_{ij}^f	Reactive power flowing on transmission line (ij) [MVAR]
s_{ij}^f	Apparent power flowing on transmission line (ij) [MVA]
v_i	Voltage magnitude at node i [pu]
δ_i	Voltage angle at node i [rad]
$\cos\phi_i^g$	Power factor of generator connected at node i [–]
x	ANN input vector [–]
y	ANN output vector [–]
θ	ANN parameters [–]
O_h	Output of ANN hidden layer h [–]
ϕ_h	Activation function of ANN hidden layer h [–]
W_h	Weight matrix of ANN hidden layer h [–]
b_h	Bias vector of ANN hidden layer h [–]
λ	Boundary tightening parameter for voltage magnitude constraints [–]
μ	Boundary tightening parameter for line loading constraints [–]
z'_m	SHAP coalition vector m [–]
β_y	SHAP values matrix for output y [–]
lf_t	Load factor at time step t [–]
gf_t	PV generation factor at time step t [–]

congestions [6]. To handle these problems, grid operators could either acquire new network assets or adopt new operational strategies [7]. In [8], the authors show that in the case of UK's electricity grid, savings of £14.3 m by 2050 could be achieved by utilizing the reactive power capability of DGs as opposed to upgrading the grid. In Germany, the grid code dictates that all PV systems should be able to provide reactive power support by varying their power factor between 0.9/0.95 lagging and 0.9/0.95 leading, i.e., absorbing or producing reactive power as necessary [9,10].

However, individual systems are free to determine their own re-active power dispatch strategy, leading to the existence of different strategies in the literature. Existing works on the topic can be classified into two groups: rule-based and optimization-based methods [11]. Rule-based methods determine optimal reactive power dispatch in DGs by relying on locally available measurements of the grid state and pre-defined rules, among which droop control according to the IEEE 1547 Standard is the most commonly implemented [12]. Although these methods are simple and computationally inexpensive, their stability and optimality cannot be guaranteed due to their local nature. In contrast, optimization-based methods use grid-wide information such as grid topology, grid component parameters and current load and generation values to formulate and solve an optimization problem, typically referred to as the AC optimal power flow (ACOPF) or simply OPF problem. In OPF, optimal reactive power dispatch is determined according to a certain grid-wide objective such as minimizing energy losses or overall supply cost while respecting physical and operational constraints, e.g., power flow (PF) equations, line PF, transformer loading and voltage magnitude limits. In [6], the authors proposed a simultaneous optimal allocation of PV systems and adaptive reactive power control by formulating a chance-constrained stochastic programming problem. The potential of reactive power support from wind farms is explored in [13], in which a two-stage linear optimization problem was formulated to determine robust reactive power dispatch ranges bearing in mind the uncertainty of wind power generation. In [11], a two-stage model predictive control (MPC) was designed to determine optimal control actions on two different time scales: 1 h and 5 min to control capacitor banks and reactive power dispatch, respectively. A similar two-stage approach is proposed in [14] with the addition of a distributed OPF algorithm to coordinate reactive power dispatch in DGs.

Although optimization-based approaches achieve satisfying results, they are not always practical. Since PF equations are non-linear, OPF is a non-convex optimization problem which is computationally expensive to solve. Additionally, OPF assumes centralized coordinated control by the grid operator which necessitates an extensive and expensive monitoring and communication infrastructure [15]. As alternatives to centralized OPF, a number of distributed and decentralized OPF methods have been proposed in the literature. Distributed methods break down the centralized optimization problem into smaller sub-problems to be solved by individual systems and later consolidated to produce feasible setpoints [14,15], while decentralized methods assume that each system is fully responsible for their own optimal set-point by only communicating with its physically-connected neighbors without the need of a central control entity [16]. A comparison of distributed and decentralized OPF methods is presented in [17]. Both distributed and decentralized OPF methods hold several advantages over centralized OPF, in that they support data privacy preservation by reducing the amount of information exchange between systems while also enabling parallel computation [18]. However, the computational burden of OPF remains even in distributed and decentralized settings, hence machine learning (ML) methods have been implemented to solve this issue.

In machine learning-based optimal power flow (ML-OPF), ML models are trained to learn an input–output mapping between load profiles and their corresponding optimal generator set points so that the latter

voltage levels could occur during periods of high renewables production [5]. This could lead to a multitude of operational problems such as voltage and frequency fluctuations, overloading of transformers or line

can be predicted in a data-driven way, i.e., without actually solving complex optimization problems. A survey of ML-OPF applications proposed in the literature could be found in [19], which classifies existing applications into five categories: (1) direct mapping of OPF solutions, (2) predicting active constraints, (3) mapping binary decision variables, (4) learning OPF control policy and (5) predicting warm-start points. The first two applications are first explored in [20] using artificial neural network (ANN). Direct mapping of OPF solutions is also used in [21], in which the authors proposed pre- and post-processing procedures to ensure the feasibility of ML-OPF solutions. Similarly, the authors in [22] proposed the use of dual Lagrangian method to penalize OPF constraint violations and drive ML-OPF solutions towards feasible solution space. In [23], reinforcement learning is used to derive ANN for solving standard OPF and grid congestion management problems guided by learning policies obtained from PF equations.

In this paper, we propose the use of machine learning to leverage ML-OPF for reactive power control. Bearing in mind the highly fluctuating nature of PV generation, ML-OPF allows for more fine-grained control of reactive power in PV systems by finding optimal set points almost instantaneously and enabling control to be administered with higher frequency, e.g., close to real-time. The main contributions of this paper are as follows:

- We propose to use ANN to provide an end-to-end prediction of optimal reactive power dispatch in PV systems from entire grid state measurements. To this end, we trained an ANN to learn a mapping between nodal loads and PV active powers (input) and optimal PV reactive powers obtained by solving standard ACOPF (output), i.e., replacing ACOPF with a less computationally expensive ANN to perform centralized control of reactive power in PV systems. Existing studies with similar focus on ML for reactive power control have only sought to predict optimal reactive power dispatch from local measurements [24–26]. Furthermore, none of the existing ML-OPF studies have explored the use of the learning paradigm to optimize reactive power dispatch [20–22]. Hence, in this paper we show that it is possible to perform centralized control of reactive power dispatch in PV systems using ML-OPF with satisfactory results.

- We utilize Shapley Additive Explanations (SHAP) [27], an explainable artificial intelligence (XAI) technique, to provide further insights into the behavior of the centralized ANN controller. SHAP generates feature importances, i.e., it identifies relevant grid state measurements for each PV system when determining their optimal reactive power output. Based on this knowledge, we trained smaller ANNs, one for each PV system, to act as decentralized controllers. These smaller ANNs are trained only on a subset of the centralized controller's features, i.e., in addition to the local measurements, they are only allowed access to certain measurements from other nodes. This allows each system to determine its own optimal set point given partial knowledge of the grid state and eliminates the need for centralized coordination. To the best of our knowledge, none of the existing studies have looked into the possibility of using SHAP in this context. Moreover, decentralized reactive power control using only local measurements was shown to cause small constraint violations during operation [24]. We aim to demonstrate SHAP's capability to provide highly relevant information which could then be used to build ANN-based decentralized controllers with all the corresponding advantages with no perceivable loss in performance compared to their centralized counterpart.

The rest of this paper is organized as follows: Section 2 provides an overview of the tools and methods used in this paper, while Section 3 covers the results obtained and the corresponding interpretation and discussion. Finally, conclusions drawn from the results as well as an outlook for future research are presented in Section 4.

2. Methodology

In this section, descriptions of the relevant methods covering standard ACOPF formulation and the use of ANN and XAI for ACOPF are provided. Additionally, an overview of the case study built to showcase the merits of the proposed ML-OPF paradigm as well as the steps taken to derive the subsequent results are presented.

2.1. AC optimal power flow (ACOPF) problem for reactive power control

The standard ACOPF formulation is described below. For a fixed grid topology, let N denote the set of nodes (buses), L the set of edges (lines), $D \subseteq N$ the set of loads (demands) and $G \subseteq N$ the set of controllable generators. Furthermore, let p_i^g and q_i^g represent the active and reactive power generation at node i, respectively, while p_i^d and q_i^d represent the active and reactive power load. The active and reactive power flowing on the transmission line $(ij) \in L$ connecting buses i and j are denoted by p_{ij}^f and q_{ij}^f, respectively. Meanwhile, let v_i and δ_i denote the voltage magnitude and voltage angle at node i. The ACOPF problem can then be formulated as follows:

$$\underset{p_i^g, v_i}{\text{minimize}} \quad \sum_{i \in G} C_i(p_i^g) \tag{1a}$$

subject to

$$p_i^{g,min} \leq p_i^g \leq p_i^{g,max} \forall i \in G \tag{1b}$$

$$q_i^{g,min} \leq q_i^g \leq q_i^{g,max} \forall i \in G \tag{1c}$$

$$v_i^{min} \leq v_i \leq v_i^{max} \forall i \in N \tag{1d}$$

$$\delta_i^{min} \leq \delta_i \leq \delta_i^{max} \forall i \in N \tag{1e}$$

$$p_i^g - p_i^d = \sum_{(ij) \in L} p_{ij}^f \forall i \in N \tag{1f}$$

$$q_i^g - q_i^d = \sum_{(ij) \in L} q_{ij}^f \forall i \in N \tag{1g}$$

$$\sqrt{(p_{ij}^f)^2 + (q_{ij}^f)^2} \leq s_{ij}^{f,max} \forall (ij) \in L \tag{1h}$$

The objective is to determine the optimal generator active power outputs p_i^g and voltage set points v_i so as to minimize the overall cost of active power generation according to (1a), where $C_i()$ denotes the cost function of the generator at node i. Constraints (1b) and (1c) limit all generator active and reactive power outputs to be within their physical limits as given by $[p_i^{g,min}, p_i^{g,max}]$ and $[q_i^{g,min}, q_i^{g,max}]$, respectively. Meanwhile, voltage magnitudes v_i and angles δ_i also have to be kept inside a certain range $[v_i^{min}, v_i^{max}]$ and $[\delta_i^{min}, \delta_i^{max}]$ as dictated by constraints (1d) and (1e). Constraints (1f) and (1g) represent nonlinear PF equations used to calculate the active and reactive power flowing on the transmission lines p_{ij}^f and q_{ij}^f and enforce energy conservation in accordance with Kirchhoff's current law. Finally, constraint (1h) restricts the apparent power flowing on the transmission lines to not exceed the physical limits as dictated by the lines' specifications. Note that ACOPF is always solved assuming the presence of a slack bus $s \in N$ whose voltage magnitude and angle are set to a certain value, e.g., $v_s = 1.0$ pu and $\delta_s = 0$.

For reactive power control, we assume that only PV generators are present, which is usually the case in medium-voltage (MV) distribution grids. No voltage set points could be determined in PV generators, rather only the reactive power outputs of the generators q_i^g. Accordingly, the ACOPF problem should be reformulated as follows:

$$\underset{q_i^g}{\text{minimize}} \quad C_s(p_s^g) \tag{2a}$$

subject to

(1d) – (1h)

$$p_i^g = p_i^{g,current} \qquad \forall i \in G \tag{2b}$$

$$q_i^{g,min} \leq q_i^g \leq q_i^{g,max} \quad \forall i \in G \tag{2c}$$

Hence, the objective now is to minimize the active power imported from the high-voltage (HV) transmission grid assumed to be connected at the slack bus s as shown in (2a). Through constraint (2b), we assume that the active power generation from PV generators cannot be curtailed and the active power generated at each time instant $p_i^{g,current}$ has to be accommodated. Constraint (2c) dictates the admissible reactive power generation from the PV generators q_i^g by setting a bounding box $[q_i^{g,min}, q_i^{g,max}]$, which depends on the current active power $p_i^{g,current}$ and the maximum allowable inverter power factor $\cos\phi_i^{g,max}$. Active and reactive power are related through the power factor according to the following set of equations:

$$p_i^g = s_i^g \cdot \cos\phi_i^g \tag{3}$$

$$q_i^g = s_i^g \cdot \sin\phi_i^g \tag{4}$$

$$s_i^g = \sqrt{(p_i^g)^2 + (q_i^g)^2} \tag{5}$$

$$q_i^g = p_i^g \cdot \tan\phi_i^g, \tag{6}$$

where s_i^g denotes the apparent power flowing from the PV system. The power factor could be set to either leading or lagging depending on whether the system is needed to absorb or produce reactive power, respectively. Hence, the relationship between reactive power generation limits, maximum power factor and current active power is described as follows:

$$q_i^{g,min} = -p_i^{g,current} \cdot \tan\phi_i^{g,max} \tag{7}$$

$$q_i^{g,max} = p_i^{g,current} \cdot \tan\phi_i^{g,max} \tag{8}$$

We assume that inverters on the PV systems are sufficiently oversized to admit the required apparent power at peak PV active power generation $p_i^{g,peak}$, e.g., for $\cos\phi_i^{g,max} = 0.9$ the required inverter capacity p_i^{inv} would be equal to $\frac{1}{0.9} \cdot p_i^{g,peak} = 1.11 \cdot p_i^{g,peak}$. Oversizing PV inverters in this way has been shown to be effective in preventing voltage problems in grids with high renewables penetration [28,29].

2.2. Artificial neural network (ANN) for ACOPF

ANNs are known to be high-performing approximators of nonlinear mappings. Given an input vector $x \in \mathbb{R}^{|X|}$ and its corresponding output vector $y \in \mathbb{R}^{|Y|}$, ANN learns a mapping function $f(x, \theta) = \hat{y}$, where θ denotes the parameters of the ANN, such that the distance between y and $\hat{y}$ is minimized. In practice, ANN represents $f(x, \theta)$ as a series of nonlinear operations referred to as hidden layers given by:

$$O_h = \sigma_h(W_h \cdot O_{h-1} + b_h) \mid h \in [1, 2, \ldots, H + 1], \tag{9}$$

where the subscript h indicates the position of the hidden layer, H the number of hidden layers, $W_h \in \mathbb{R}^{n_h \times n_{h-1}}$ the weight matrix in layer h, $b_h \in \mathbb{R}^{n_h}$ the bias vector in layer h, O_{h-1} the output of the previous hidden layer and σ_h a nonlinear function referred to as activation function in layer h. n_h denotes the number of neurons in layer h, which is a tunable parameter. Taking $O_0 = x$ and $n_{H+1} = |Y|$ allows us to obtain $\hat{y}$ as the output of the last hidden layer, i.e., O_H. As seen in (9), ANN parameters θ consist of the weight matrices and bias vectors $W_h, b_h \forall h \in [1, 2, \ldots, H]$, which have to be derived through a learning process. Given a dataset of $|K|$ input–output pairs $\{(x_1, y_1), \ldots, (x_k, y_k)\}$, the learning process minimizes a loss function $\mathcal{L}_o$ which can be chosen based on the task at hand. For regression tasks, a simple loss function such as mean squared error is usually used, which entails representing the learning process as the following optimization problem:

$$\underset{\theta}{\text{minimize}} \quad \mathcal{L}_o = \frac{1}{K} \sum_{k=1}^{K} \|y_k - f(x_k, \theta)\|^2 \tag{10}$$

In this paper, an ANN is used to learn a mapping between grid states in the form of nodal loads and PV active powers and optimal settings in the form of PV reactive powers by modeling ACOPF as a regression task. For a fixed grid topology with $|D|$ connected loads and $|G|$ connected

PV generators, the input to the ANN is the vector $x \in \mathbb{R}^{|D|+|G|}$, which is the concatenation of all current loads and PV active powers, i.e., $(p_i^d, p_j^g) \forall i \in D, j \in G$. Meanwhile, the output is the vector $y \in \mathbb{R}^{|G|}$ representing the optimal PV reactive powers, i.e., $q_i^g \forall i \in G$. To generate a dataset of $|K|$ training samples for the ANN, loads and PV active powers are simultaneously varied to obtain $|K|$ variations of the grid state, reflecting their dynamic nature. Subsequently, the corresponding optimal PV reactive powers for each variation are obtained by solving the ACOPF optimization shown in (2b), hence creating $|K|$ input–output pairs $\{(x_1, y_1), \ldots, (x_k, y_k)\}$.

ANN is a function providing a numerical approximation which might produce infeasible solutions to the original ACOPF problem. Since the ANN is only used to predict the PV reactive powers q_i^g, the remaining state variables, i.e., voltage magnitudes v_i the power flowing on the transmission lines p_i^f have to be recovered by plugging the predictions into the nonlinear PF equations (1f) and (1g). However, the following problems might be encountered when using ANN-derived solutions:

- The predicted outputs $\hat{q}_i^g$ might be outside the boundaries dictated by constraint set (2c).
- The recovered voltage magnitudes v_i and power flowing on the transmission lines p_i^f might violate constraints (1d) and (1h), respectively.

To avoid these problems, we adopted a strategy inspired by [21] to ensure the feasibility of ANN-derived solutions. For the first problem, note that Eqs. (7) and (8) dictate the reactive power limits to be symmetric. Hence, dividing constraint (2c) by $q_i^{g,max}$ yields:

$$-1 \leq \frac{q_i^g}{q_i^{g,max}} \leq 1, \tag{11}$$

where $\frac{q_i^g}{q_i^{g,max}}$ could be interpreted as the fractions of available reactive power actually produced (> 0) or absorbed (< 0). These fractions are then used in the place of q_i^g as outputs of the ANN. By using a suitable activation function in the last layer, i.e., tanh, the outputs of the ANN could be squashed to $[-1, 1]$, therefore ensuring that the solutions produced by the ANN are always admissible.

Meanwhile, to address the second problem, it is necessary to ensure that the ANN does not learn solutions that are located on the constraint boundaries, e.g., $v_i = v_i^{min}$ or $\sqrt{(p_{ij}^f)^2 + (q_{ij}^f)^2} = S_{ij}^{f,max}$ for $i \subseteq N$. Hence, we introduce two parameters λ and μ, which act as boundary tightening parameters for voltage magnitude limit and line loading limit, respectively. Accordingly, we solve the following restricted ACOPF problem to generate training samples for the ANN:

$$\underset{q_i^g}{\text{minimize}} \quad C_s(p_s^g) \tag{12a}$$

subject to

$$\text{(1e) – (1g), (2b), (2c)}$$

$$v_i^{min} + \lambda \leq v_i \leq v_i^{max} - \lambda \quad \forall i \in N \tag{12b}$$

$$\sqrt{(p_{ij}^f)^2 + (q_{ij}^f)^2} \leq \mu \cdot s_{ij}^{f,max} \quad \forall (ij) \in L \tag{12c}$$

The resulting outputs of the restricted ACOPF problem deviate from the original ACOPF mapping because of the tightening of the constraint boundaries, which might result in inferior solutions with regard to the objective function. Hence, the parameters λ and μ induce an optimality-feasibility trade-off, i.e., larger λ values and smaller μ values should ensure feasibility while degrading the objective function value and vice-versa. However, it is also important to note that when either λ is too large or μ is too small, the restricted ACOPF problem might become infeasible and no optimal solution could be found. In this paper, we set $\lambda = 0.0025$ and $\mu = 0.95$, which were determined empirically to produce strictly feasible solutions with negligible optimality loss.

2.3. Explainable artificial intelligence (XAI) for ACOPF

In this paper, we use SHAP, a model-agnostic XAI technique to generate explanations in the form of feature importance values from ANN. In SHAP's terminology, feature importance values are calculated as Shapley values from coalitional game theory. Accordingly, SHAP treats the input of an ANN as players in a game, which could either be playing ("present") or not playing ("absent").

To represent the input as such, binary arrays (coalitions) $z' \in \{0,1\}^{|X|}$ are generated, where $|X|$ is the number of input features. These arrays are subsequently used as masking arrays for the input: features masked with 1 ("present" features) retain their original values and the values of the features masked with 0 ("absent" features) are replaced by random values of the corresponding features sampled from the data set (background samples), creating hypothetical samples. For each coalition, multiple hypothetical samples are generated so as to avoid sampling bias and approximate truly random samples. Next, these hypothetical samples are passed to the ANN to obtain the predictions, which are subsequently averaged within coalitions to obtain one average prediction value per coalition. Finally, we obtain coalition-output value pairs which are then used to fit a linear model to derive the average influence of each feature being "present" or "absent" on the output, i.e., the feature importance values.

Given a data set of $|K|$ input–output pairs $\{(x_1, y_1), \dots, (x_k, y_k)\}$ with $x \in \mathbb{R}^{|X|}$ and $y \in \mathbb{R}^{|Y|}$ and an ANN $f(x, \theta)$ as described in Section 2.2, calculating the SHAP values $\beta_u \in \mathbb{R}^{|X| \times |Y|}$ for an observation (x_u, y_u) entails:

1. Creating $|M|$ coalitions $z'_m \in \{0,1\}^{|X|}$ to create a coalition set M
2. For each coalition z'_m:

   - Calculate coalition weight $\pi_x(z'_m)$ with the SHAP kernel

$$\pi_x(z'_m) = \frac{|X| - 1}{\binom{|X|}{|z'_m|} |z'_m| (|X| - |z'_m|)}, \qquad (13)$$

   where $|z'_m|$ denotes the number of present features (1's) in z'_m

   - Repeat p times:

     – Map z'_m into the original input feature space to create a hypothetical sample: $h_x(z'_m)|_{z'_m=1} = x_u$, $h_x(z'_m)|_{z'_m=0} = x_v$, where v is sampled randomly from $\{1, 2, \dots, k \mid v \neq u\}$

     – Calculate ANN prediction for the hypothetical sample $\hat{y}_{z'_m} = f(h_x(z'_m), \theta)$

   - Calculate average ANN prediction for the coalition $y^-_{z'_m}$ by averaging over p runs

$$y^-_{z'_m} = \frac{\sum_{r=1}^{p} \hat{y}_{z'_m}}{p} \qquad (14)$$

3. Fitting linear model $g(\cdot)$:

$$g(z'_m) = \beta_0 + z'_m \cdot \beta_u \qquad (15)$$

   by minimizing the sum of squares loss (16) over the coalition set M

$$\begin{aligned} \text{minimize} \quad & \sum_{m \in M} [u^-_{z'_m} - g(z'_m)]^2 \pi_x(z'_m) \\ \text{subject to} \quad & g(z'_m) = y_u \forall m \in M \left| |z'_m| = |X| \right. \end{aligned} \qquad (16)$$

Repeating the process for all $|K|$ observations yields a distribution of SHAP values over all possible input values in the data set which provides a global explanation of the ANN's behavior. In the case of reactive power control, calculating the SHAP values distribution enables the quantification of the impact of loads p_i^d and PV active powers p_i^g on the corresponding optimal PV reactive powers q_i^g, i.e., which grid state information has significant influence on the optimal reactive power

Table 1
Summary of nominal nodal loads and installed PV capacities for the case study.

Node	$p_i^{d,nom}$ (MW)	$q_i^{d,nom}$ (MVar)	$p_i^{g,peak}$ (MW)
0	–	–	–
1	19.84	4.64	–
2	–	–	–
3	0.5	0.21	1
4	0.43	0.11	0.86
5	0.73	0.18	1.46
6	0.55	0.14	1.1
7	0.08	0.05	–
8	0.59	0.15	1.17
9	0.57	0.36	1.15
10	0.54	0.16	1.09
11	0.33	0.08	0.66

dispatch of each PV system. For example, the optimal setting of a PV system at node i might depend on the load at node $j \neq i$, p_j^d. This type of information is particularly important when moving from centralized to decentralized control paradigm, as it enables to determine strictly relevant information to be communicated with and supplied to each PV system's controller, hence reducing both the required bandwidth of the overall communication infrastructure and the computational burden on the individual controllers.

2.4. Case study

In this paper, a case study based on the CIGRE MV distribution grid [30] is developed. A schematic of the grid is shown in Fig. 1. The grid has a radial structure and consists of 12 buses with 10 connected loads ($|D|$), 8 PV systems ($|G|$), 10 transmission lines and a transformer which connects the grid to the HV transmission grid. For the purpose of our case study, the following changes were made to the initial grid model:

- Feeder line 2 was removed because no PV system was installed on the line.
- Wind turbine installed at node 8 was removed.
- At each node where PV is present, the PV installed capacity was set to be twice the nominal nodal load, representing 200% PV penetration level as measured by installed capacity.

A summary of the nominal nodal loads and installed PV capacities is shown in Table 1. To generate grid state variations reflecting its fluctuating nature, p_i^d and $p_i^{g,current}$ were generated by perturbating $p_i^{d,nom}$ and $p_i^{g,peak}$ as follows:

$$p_i^d \sim Uniform(0.4 \cdot p_i^{d,nom}, 1.3 \cdot p_i^{d,nom}) \qquad (17)$$

$$p_i^{g,current} \sim Uniform(0.4 \cdot p_i^{g,peak}, 1.3 \cdot p_i^{g,peak}) \qquad (18)$$

We assume that the loads in all the nodes have a constant power factor, i.e., the reactive loads q_i^d can be calculated as follows:

$$q_i^d = \frac{p_i^d}{p_i^{d,nom}} \cdot q_i^{d,nom} \qquad (19)$$

Plugging p_i^d, q_i^d and $p_i^{g,current}$ into the restricted ACOPF problem formulation shown in (12b) and additionally setting v_i^{min} and v_i^{max} to 0.95 and 1.05 pu, respectively, leads to a complete definition of the optimization problem. We solved the nonlinear optimization problem using the open-source Interior Point Optimizer (Ipopt) [31] solver integrated in pandapower [32] and PowerModels [33]. As training data for the ANN, 50,000 samples ($|K|$) were generated and solved to obtain the corresponding optimal PV reactive power dispatch for each sample, i.e., each grid state variation.

Using the generated samples, an ANN was trained to predict the solutions to the restricted ACOPF problem. Fig. 2 depicts the structure of the ANN used to learn the mapping function for reactive power
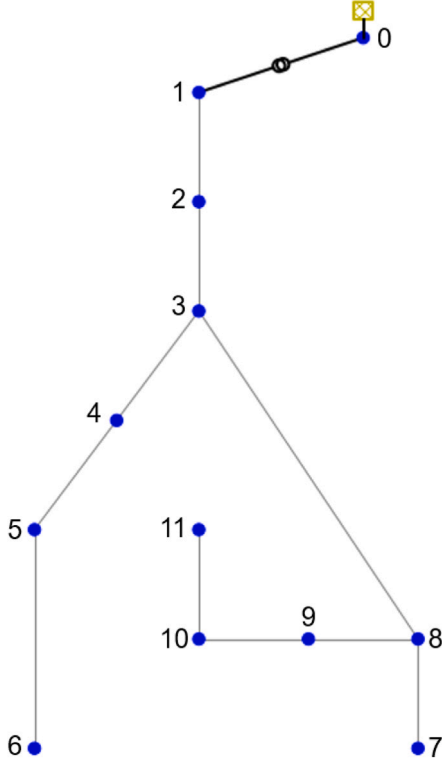
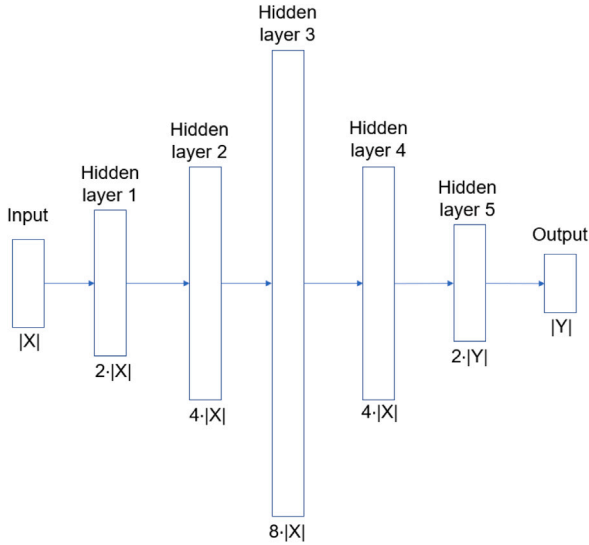**Fig. 1.** Schematic of CIGRE MV distribution grid.

Fig. 2. Proposed ANN structure for reactive power control.

control. The ANN has 5 hidden layers and the number of neurons in each layer, shown below the layer depiction, was determined as such to create a decoder–encoder structure as proposed in [22]. For our case study, $|X|$ is equal to 18 and $|Y|$ is equal to 8. All hidden layers use the rectified linear unit (ReLU) activation function and the output layer uses tanh activation function to ensure admissible outputs as described in Section 2.2. The ANN was implemented using TensorFlow [34] and Keras [35] and trained using the Adam optimizer [36]. The learning rate and the maximum number of epochs during training were set to 0.001 and 100, respectively. The ANN was trained using 80% of the samples generated as described previously and the remaining 20% were set aside for testing.

Let the sets X, Y and S represent the ANN's input feature set, output set and samples set, respectively. Once a trained ANN with satisfactory performance was obtained, SHAP was used to generate feature importance values. Accounting for the number of samples, the full set of SHAP values obtained is a tensor $\beta \in \mathbb{R}^{|K| \times |X| \times |Y|}$. Since our objective is to determine the set of important features for each output, we sliced the tensor over the third dimension to obtain $|Y|$ matrices $\{\beta_1, \ldots, \beta_y\} \in \mathbb{R}^{|K| \times |X|}$, each representing the distribution of feature importance values of each feature for the corresponding output. Each element in the matrix $\beta_{y(k,x)}$ represents the feature importance value of feature x with regard to output y for sample k. First, we calculated the mean absolute feature importance value for each output across all samples and input features as given by:

$$\bar{\beta}_y = \frac{\sum_{k \in K} \sum_{x \in X} |\beta_{y(k,x)}|}{|K| \cdot |X|}, \tag{20}$$

which will then be used as a threshold to indicate whether a feature is deemed as important. Correspondingly, we calculated the per-feature mean absolute feature importance values as follows:

$$\bar{\beta}_{y(x)} = \frac{\sum_{k \in K} |\beta_{y(k,x)}|}{|K|}, \tag{21}$$

which is equivalent to taking the absolute values of each column in β_y and averaging them, yielding $|X|$ mean values. Lastly, we determined the subsets of important input features $P_y \subseteq X \big| \bar{\beta}_{y(p)} \geq \bar{\beta}_y$ for all $y \in Y$. These features are subsequently used to build decentralized controllers.

Since each output $y \in Y$ represent one PV system connected to the grid, an ANN was built for each system using the subsets of important features P_y identified above. This way, each system has its own individual controller and does not depend on the centralized ANN controller any longer to determine its optimal reactive power dispatch. The same ANN structure as shown in Fig. 2 was kept but the numbers of neurons in the hidden layers were fixed to $\{32, 128, 256, 128, 32\}$. The training samples used to train the centralized ANN were also used to train the decentralized ANNs. However, note that each decentralized ANN has only one output and uses important feature subsets P_y instead of the full feature set X as input so the samples were adjusted accordingly before training. The learning rate, maximum number of epochs and train-test split configurations from the centralized ANN were maintained for the training process of the decentralized ANNs.

To analyze the marginal value of additional grid state measurements for decentralized controllers, we conducted a sensitivity analysis. For the baseline, we consider the case in which all decentralized controllers only have access to local measurements, e.g., the ANN controller for q_8^g only has p_8^d and p_8^g as input features and so on. For each system, i.e., output $y \in Y$, we took the per-feature mean absolute feature importance values $\bar{\beta}_{y(x)}$ calculated previously and sorted them in a descending manner, i.e., ranking the input features from most to least important. After removing the local measurements from the full set of input features, the sensitivity analysis was subsequently conducted by adding the next most important feature for each system to its current input feature set, training new decentralized ANNs with these expanded input feature sets and evaluating the ANNs' performance. The whole train-evaluate-expand loop was conducted for $|X| = 2$ (baseline, local measurements only) to 10. For the sensitivity analysis, the learning rate and train-test split configurations were carried over as described previously, whereas the maximum number of epochs was reduced to 30 to ease some of the computational burden.

All proposed ANNs were tested with load and PV generation profiles typical for Germany. The load profile was obtained from the ENTSO-E Transparency Platform [37], which provides the total electricity load in the transmission grid of European countries in 15-minute resolution. For this purpose, the German grid's load profile for the year 2021 was retrieved and was subjected to the following preprocessing steps:

- The annual average 15-minute loads for each timestep, e.g. 00:00, 00:15, ..., 23:45, was calculated to derive typical load fluctuations throughout the day.
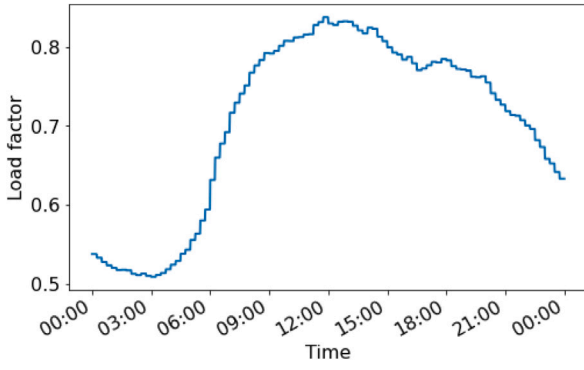
Fig. 3. Load factor time series over a typical day.

Fig. 4. PV generation factor time series over a typical day.

- The resulting 15-minute loads were subsequently upsampled to 1-minute resolution assuming constant load inside each 15-minute period.
- Finally, the 1-minute loads were normalized by the annual peak load to yield load factors, i.e., ratios of the actual load inside each 1-minute period to the peak load.

The derived evolution of the load factor throughout a typical day is depicted in Fig. 3. It could be seen that between midnight and early morning, the load factor stays largely constant at around 0.53 before rising constantly starting from around 04:00 in the morning and reaching its peak of approximately 0.85 around noon. From then on, the load factor is mostly stable for a few hours before slowly dropping off towards the evening.

Meanwhile, the PV generation profile was retrieved for a PV system located in Berlin (latitude 52.47357°, longitude 13.40332°). Since we would like to have a high-resolution PV generation profile, an irradiance time series with 1-minute resolution for the year 2017 was generated as described in [38] and provided online in [39]. The provided time series was subsequently preprocessed as follows:

- All irradiance values were divided by 1000 W/m² to yield PV generation factors, i.e., ratios of the actual generation to the peak power. We assume that the power generated by PV systems depends only on the available irradiance and the relationship between the generated power and irradiance is linear. Since PV systems can only generate up to their peak power, generation factor values above 1 were truncated so that the maximum PV generation factor in the time series is equal to 1.
- To simulate the capability of reactive power control to cope with significant PV generation fluctuations, the PV generation profile for a partly cloudy summer day was chosen.

The resulting PV generation factors are shown in Fig. 4. It could be seen that on this particular day, the PV generation factors are in general high although they fluctuate significantly, indicating a sunny day with scattered clouds. More importantly, at some points in the day, the PV generation factor is equal to 1, i.e., during this period PV systems are generating at their peak power, which might lead to voltage and stability issues in a grid with high PV penetration as considered in our case study.

The obtained load factors lf_t and PV generation factors gf_t for all $t \in T$ representing 1-minute time steps over an entire day were used to perform a closed loop evaluation of reactive power control strategies. For each time step, the load factors and the PV generation factors are multiplied with the nominal nodal loads and the installed PV capacities, respectively, to obtain the current nodal load and PV active power generation:
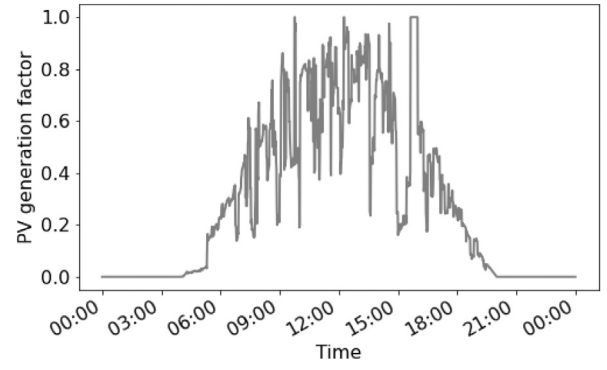
$$p_i^d = lf_t \cdot p_i^{d,nom} \tag{22}$$

$$p_i^{g,current} = gf_t \cdot p_i^{g,peak}, \tag{23}$$

while the assumed constant load power factor allows q_i^d to be calculated using Eq. (19). Using the optimal reactive powers q_i^g obtained from controllers leads to a completely defined PF problem which has to be solved to retrieve the remaining state variables as described in 2.2. The following metrics are used to evaluate the performance of the controllers:

- Total electricity imported from the transmission grid (η_1): the ACOPF's objective function to be minimized as defined in (2b), summed over the entire evaluation period of one day and converted to MWh.

$$\eta_1 = \frac{\sum_{t \in T} p_s^g}{60} \tag{24}$$

- Voltage violation count (η_2): the number of time steps (or minutes) constraint (1d) is violated for the evaluation period.

$$\eta_2 = \sum_{t \in T} |t| \forall t \in T \Big| v_i > v_i^{max} \lor v_i < v_i^{min}, i \in N \tag{25}$$

- Mean voltage violation (η_3): the average violation magnitude of constraint (1d) in pu.

$$\eta_3 = \frac{\sum_{t \in T} \sum_{i \in N} \max\Big(\max(v_i - v_i^{max}, 0), \max(v_i^{min} - v_i, 0)\Big)}{|T| \cdot |N|} \tag{26}$$

- Maximum voltage violation (η_4): the maximum violation magnitude of constraint (1d) in pu.

$$\eta_4 = \max\Bigg(\max\Big(\max(v_i - v_i^{max}, 0), \max(v_i^{min} - v_i, 0)\Big)$$
$$\forall t \in T, i \in N\Bigg) \tag{27}$$

- Line loading violation count (η_5): the number of time steps (or minutes) constraint (1h) is violated for the evaluation period.

$$\eta_5 = \sum_{t \in T} |t| \forall t \in T \Big| s_{ij}^f > s_{ij}^{f,max}, (ij) \in L \tag{28}$$

To compare our proposed approach with existing approaches, we consider two baseline control strategies and one alternative decentralized control strategy for reactive power control. In total, we compared six approaches as described below:

1. Fixed power control (s1): according to this strategy, a constant power factor of 0.9 (lagging) is used by all PV systems, i.e., as much reactive power as possible is absorbed by each PV system. In theory, this should eliminate most overvoltage problems as voltage magnitudes sink at nodes where reactive power is imported.

2. Power factor as a function of active power ($\cos\phi(P)$) control (s2): according to the standard set by the German association VDE [10], PV systems should operate with a unity power factor when they operate below than or at half of their peak power and beyond that, the power factor should drop gradually so that a linear degradation to a power factor of 0.9 (lagging) is achieved when the peak power is reached.

3. ACOPF (s3): optimal reactive powers obtained by solving the optimization problem shown in (2b). This is the state-of-the-art strategy for reactive power control and represents the upper limit of the performance level ML-OPF based controllers can achieve since training samples for the latter are generated from ACOPF.

4. Centralized ANN (s4): an ANN with 5 hidden layers as shown in 2 with all grid state measurements as input and all PV reactive powers as output.

5. Decentralized ANN (s5): smaller ANNs to administer optimal reactive power setting for all PV systems, one for each system. Each ANN has one output and varying number of input features as identified by SHAP from the centralized ANN.

6. Multiple linear regression with local measurements (s6): the control strategy proposed in [40]. The controller is a multiple linear regression model with interactions using only local measurements.

3. Results and discussion

In this section, the results of the case study are presented and discussed. The section is divided into four subsections as follows: Section 3.1 compares the performance of the first four control strategies, i.e., baseline and centralized approaches, Section 3.2 contains an analysis of the SHAP values obtained from centralized ANN, Section 3.3 presents a comparison of the two considered decentralized control strategies and Section 3.4 shows the results of the sensitivity analysis.

3.1. Baseline and centralized control

Results of the closed loop evaluation for the baseline and centralized controllers are summarized in Table 2. Firstly, it could be seen that with regard to η_1, the ACOPF control (s3) records the best performance, followed by the centralized ANN (s4), the $\cos\phi(P)$ control (s2) and lastly the fixed power control strategy (s1). Since the performance of the centralized ANN is very similar to the ACOPF control, it could be said that the two controllers are equal, i.e., the centralized ANN successfully learned the input–output mapping of the ACOPF which minimizes the objective function of the latter. Between the best controller (s3) and the worst (s1), a difference of 1.54 MWh can be observed, meaning that switching from the fixed power control strategy to using ACOPF for controlling reactive power yields an energy saving of 0.44% over the course of the evaluated day. A similar amount of energy saved is observed when centralized ANN is deployed and although a saving of 0.44% might seem trivial, the size of the grid should be taken into account when evaluating the magnitude of the savings. For example, the average daily load of the German electricity grid in 2021 is equal to 5528 GWh [37], which means that a saving of 0.44% would be equal to 24.33 GWh.

With regard to the voltage-related metrics η_2, η_3 and η_4, all controllers successfully prevented voltage problems from occurring in the grid by applying their respective strategy. The voltage profiles at node 3 and 11, representing the first and the last node on the grid where PV is installed, are shown in Figs. 6 and 7. From the figures, it could be seen that the ACOPF controller and the centralized ANN provide optimal reactive power settings as such to absorb just enough reactive power to keep the voltage at or close to the upper limit when high PV generation is observed. There is a small difference between the voltage profiles of the ACOPF and the centralized ANN, which could be attributed to the

Table 2
Summary of evaluation results for the baseline and centralized controllers.

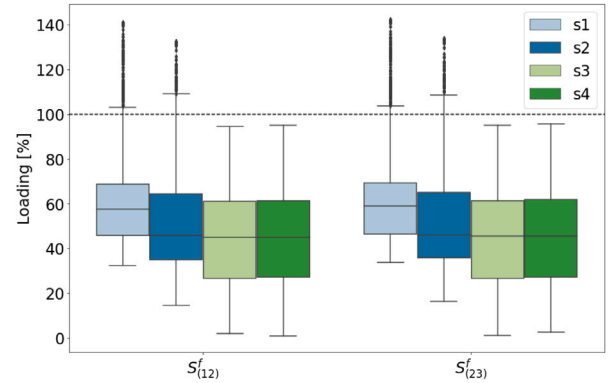| Controller	η_1 [MWh]	η_2 [min]	η_3 [pu]	η_4 [pu]	η_5 [min]
s1	353.58	0	0	0	218
s2	352.75	0	0	0	98
s3	352.05	0	0	0	0
s4	352.06	0	0	0	0

Fig. 5. Distribution of loading values in percentage for lines (12) and (23).

fact that the latter was trained using samples generated from solving the reduced ACOPF problem where the constraints are tightened. In contrast to the more complex controllers, the baseline controllers instruct more reactive power to be absorbed during the same period, leading to voltages far below the upper limit.

When it comes to η_5, however, both the fixed power and the $\cos\phi(P)$ controllers perform poorly, recording 218 and 98 min of line loading violations, respectively. This might be caused by the controllers instructing the PV systems to absorb more reactive power than necessary, subsequently leading to overloading of the transmission lines. The excessive absorption of reactive power is also likely to be the reason behind both baseline controllers' inferior performance since increasing energy flowing on the transmission lines also leads to higher losses. In reality, the line loading limits cannot physically be exceeded so once the power flowing on a transmission line is detected to approach the maximum capacity, i.e., a congestion is about to occur, grid operators would need to dispatch control measures to clear the congestion which incur additional system costs. Fig. 5 shows the distribution of line loading values for the transmission lines connecting nodes 1 and 2 and nodes 2 and 3, where the congestions occur.

On the whole, it could be said that both ACOPF and centralized ANN are superior to the evaluated baseline controllers for controlling reactive power in PV systems with regard to all the metrics considered in this paper. Furthermore, it has been shown that the centralized ANN successfully imitates the behavior of the ACOPF controller and hence, it is possible to control reactive power in PV systems using ANNs trained with ACOPF-generated input–output mappings.

3.2. SHAP analysis for centralized ANN

Once the centralized ANN for reactive power control has been evaluated and its performance has been validated, SHAP values were calculated to generate additional insights with regard to the optimal reactive power dispatch of each PV system. The SHAP summary plots for the PV systems at node 3 and 11 are shown in Figs. 8 and 9. The plots depict the spread of the input features' SHAP values and their influence on the output. Note that only the five most important features to each output are shown to ease the interpretation. In Fig. 8, it could be seen that the optimal reactive power at node 3 q_3^g is mostly affected by the load at node 1 p_1^d, the load at node 3 p_3^d and the actual PV active
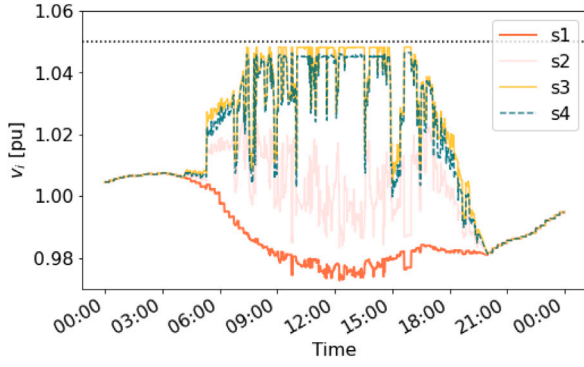
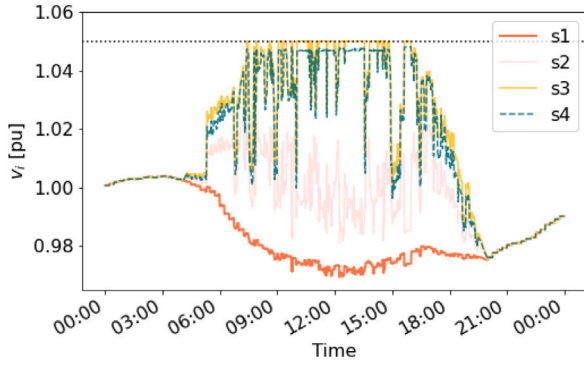**Fig. 6.** Voltage profile at node 3 for the baseline and centralized controllers.

Fig. 7. Voltage profile at node 11 for the baseline and centralized controllers.

Fig. 8. SHAP summary plot for optimal reactive power dispatch at node 3.

Fig. 9. SHAP summary plot for optimal reactive power dispatch at node 11.

Table 3
List of input features identified by SHAP for the decentralized ANN: features highlighted in bold indicate local measurements.

Output	$\bar{\beta}_y$	Input features
q_3^g	0.027	$p_1^d, \boldsymbol{p_3^d, p_3^g}$
q_4^g	0.009	$\boldsymbol{p_4^d, p_4^g}$
q_5^g	0.023	$\boldsymbol{p_1^d, p_4^g, p_5^d, p_5^g}$
q_6^g	0.06	$p_1^d, p_4^g, p_5^d, p_5^g, \boldsymbol{p_6^d, p_6^g}$
q_8^g	0.016	$p_7^d, \boldsymbol{p_8^d, p_8^g}, p_9^g$
q_9^g	0.055	$p_1^d, p_8^g, \boldsymbol{p_9^d, p_9^g}$
q_{10}^g	0.067	$p_1^d, p_8^g, p_9^g, \boldsymbol{p_{10}^d, p_{10}^g}$
q_{11}^g	0.054	$p_1^d, p_{10}^g, \boldsymbol{p_{11}^d, p_{11}^g}$

power generation at node 3 p_3^g. With regard to p_1^d and p_3^d, the correlation is positive, i.e., higher p_1^d and p_3^d lead to higher q_3^g. Since p_1^d represents the largest load in the entire grid, this behavior would be expected, as high q_3^g values indicate high reactive power production, presumably to be exported to node 1. It is rather expected that p_3^d and p_3^g are important to determine q_3^g, as they represent local measurements which have the largest influence on the voltage behavior.

The same behavior for local measurements is also observed for q_{11}^g as shown in Fig. 9, as p_{11}^g and q_{11}^d are deemed to be the most influential. The other three most important features identified are p_1^d, p_{10}^g and p_9^g. As mentioned before, p_1^d represents the largest load grid-wide, therefore partly explaining its inclusion although nodes 1 and 11 are separated by a large distance. In contrast, p_9^g and p_{10}^g represent the active power generations of the PV systems at node 9 and 10, respectively, which are in close vicinity to node 11. Hence, they indirectly influence q_{11}^g in that high generation at nodes 9 and 10 might necessitate the PV system at node 11 to absorb more reactive power in order to avoid potential overvoltage at all three nodes.

Table 3 lists the features identified by SHAP for each PV system's dedicated ANN controller alongside the threshold values used to identify them. First of all, it could be seen that the threshold value varies between PV systems and does not seem to follow any particular trend with regard to where the PV system is located in the grid, i.e., close to the beginning or the end of the feeder line. However, it is interesting to note that there seems to be a weak positive correlation between the number of important features and the threshold value, e.g., q_4^g has the lowest threshold value and the lowest number of features (2), while q_6^g has the second highest threshold value and the highest number of features (6). Furthermore, as observed previously, local measurements have a large influence on the optimal reactive power dispatch of all PV systems, as they are identified as important for each PV system. Using these feature sets, we built decentralized ANNs to allow each PV system to determine their optimal reactive power dispatch independently given access to some of the identified non-local grid measurements.
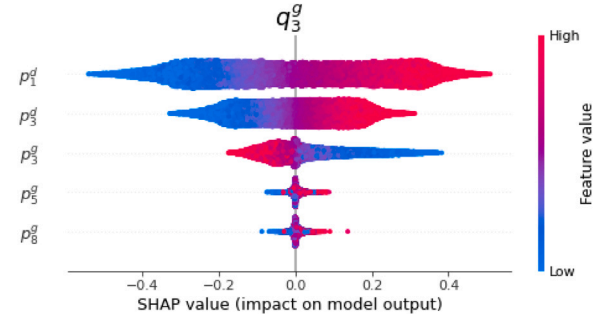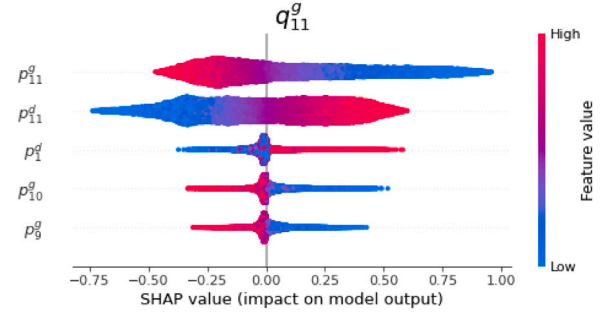
3.3. Decentralized control

Table 4 presents a comparison of the two decentralized control strategies under consideration, decentralized ANN (s5) and multiple linear regression with local measurements (s6). It could be seen that while the decentralized ANN achieves practically the same level of performance as the centralized ANN, the multiple linear regression controller induces voltage problems lasting for a total of 182 min. The voltage profiles at node 3 and 11 for these two controllers are shown in Figs. 10 and 11, respectively. From the table and the figures, it could be observed that while both the mean violation η_3 and the maximum violation η_4 are very low in the case of the multiple linear regression controller, overvoltages do occur during periods of high PV generation. As is the case with line congestions, grid operators would need to dispatch control measures to eliminate the overvoltage problem which entails additional costs. Meanwhile, the decentralized ANN controller is always able to keep the voltage below the upper limit and at the same time, no line loading violations as measured by η_5 are recorded.

The results show that for reactive power control, using only local measurements might lead to small constraint violations, which agrees with the findings in [24]. By using a combination of ACOPF input–output mapping with ANN and SHAP to identify important features, decentralized ANNs which only use a subset of grid state measurements as input are able to optimize reactive power dispatch in PV

Table 4
Summary of evaluation results for the decentralized controllers.

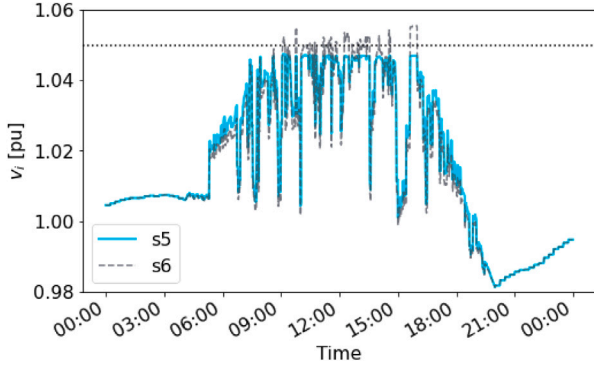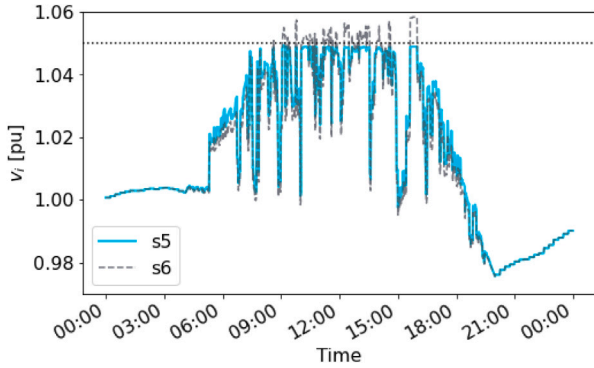| Controller	η_1 [MWh]	η_2 [min]	η_3 [pu]	η_4 [pu]	η_5 [min]
s5	352.06	0	0	0	0
s6	352.05	182	2.5e−4	8.4e−3	0

Fig. 10. Voltage profile at node 3 for the decentralized controllers.

Fig. 11. Voltage profile at node 11 for the decentralized controllers.

systems with comparable performance to the state-of-the-art ACOPF control. One concern which might be raised regarding the proposed decentralized ANN is the "unfair" treatment of the PV systems as some systems have access to more grid state measurements than others as shown in Table 3. Hence, we conducted a sensitivity analysis in which all decentralized ANNs are assumed to be granted access to the same number of grid state measurements, i.e., input features for the ANNs in order to qualitatively assess the marginal value of information for the controllers.

3.4. Sensitivity analysis

The list of important features for each PV system excluding local measurements used for the sensitivity analysis is provided in Table 5. Since the sensitivity analysis was conducted for $|X| = 2$ to 10, each output is shown as having 8 important features, ordered from the most to the least important as measured by the mean absolute SHAP value. It could be seen that with the exception of q_4^g and q_8^g, p_1^d is always identified as the most influential feature for optimal reactive power dispatch on top of the local measurements owing to its magnitude. Otherwise, no obvious trend could be identified aside from the tendency of nodes located in close vicinity having more influence on one another compared to ones separated by a large distance. For example, q_9^g is identified as being significantly influenced by p_8^g and p_8^d and q_6^g by p_5^g and p_5^d.

Table 5
List of important features for each output in decreasing order of importance per SHAP values.

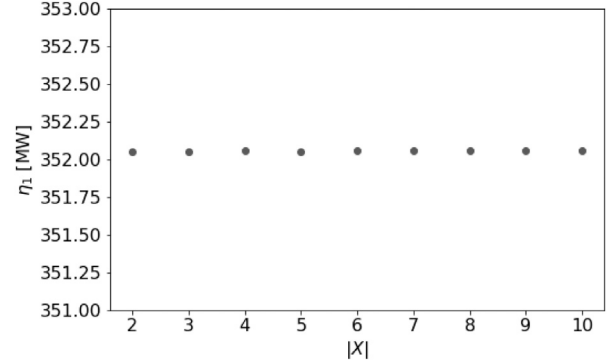| Output	Input features
q_3^g	$p_1^d, p_5^g, p_8^g, p_9^g, p_{10}^g, p_6^g, p_4^g, p_{11}^g$
q_4^g	$p_5^g, p_1^d, p_6^g, p_3^g, p_5^g, p_9^g, p_3^d, p_6^d$
q_5^g	$p_1^d, p_4^g, p_3^g, p_4^d, p_6^g, p_{10}^g, p_3^d, p_9^g$
q_6^g	$p_1^d, p_5^g, p_5^d, p_4^g, p_3^g, p_4^d, p_6^g, p_3^d$
q_8^g	$p_7^g, p_9^g, p_9^d, p_1^d, p_{10}^g, p_{10}^d, p_3^g, p_{11}^g$
q_9^g	$p_1^d, p_8^g, p_8^d, p_3^g, p_{10}^g, p_3^d, p_4^g, p_6^g$
q_{10}^g	$p_1^d, p_9^g, p_8^g, p_9^d, p_8^g, p_3^d, p_5^g, p_4^g$
q_{11}^g	$p_1^d, p_{10}^g, p_9^g, p_8^g, p_{10}^d, p_5^g, p_9^g, p_3^g$

Fig. 12. Sensitivity analysis results for η_1.

Results of the sensitivity analysis are summarized in Figs. 12 to 16. The following trends could be observed from the figures:

- η_1 is largely unaffected by the number of features in the decentralized ANNs, i.e., using only local measurements is sufficient to achieve satisfactory control performance as measured by the ACOPF's objective function.
- As is the case with the multiple linear regression controller, decentralized ANNs with only local measurements induce voltage problems. This indicates that the problem lies more in the lack of necessary information rather than model complexity.
- With one additional feature, the mean and maximum voltage violation decrease slightly but with two additional features, they are eliminated almost entirely. Four additional features for each controller are required to ensure that no voltage problem occurs.
- No line loading violations are recorded with all controllers considered in the sensitivity analysis.

From the results, it could be concluded that up to a certain point, increasing the number of features in the decentralized ANNs leads to an improvement in control performance. Once the number of features which allows for eliminating constraint violations is reached, no marginal value of information could be observed.

4. Conclusion

In this paper, we propose the use of ANN for the purpose of reactive power control in PV systems by learning approximate optimal input–output mappings from ACOPF. Through our case study, we show that ANN is able to produce optimal reactive power predictions which satisfy all grid constraints with practically the same performance as ACOPF, thereby providing an alternative to the latter for centralized reactive power control. Deploying centralized ANN controller instead of fixed power control is shown to lead to an energy saving of 0.44%. In addition to that, we show that using SHAP to generate feature importance values from the trained ANN used for reactive power control, it is possible to isolate important subsets of features which
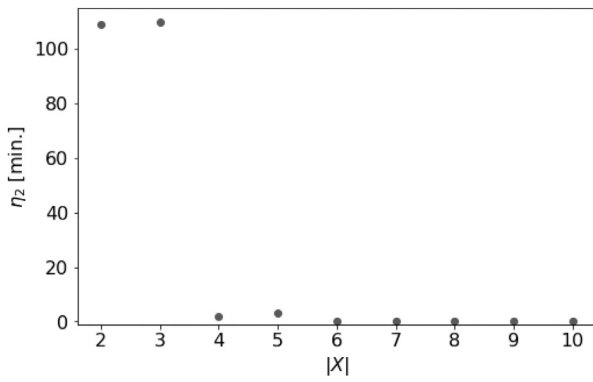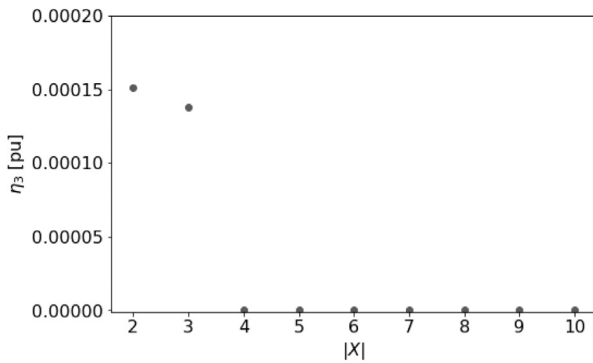
Fig. 13. Sensitivity analysis results for η_2.

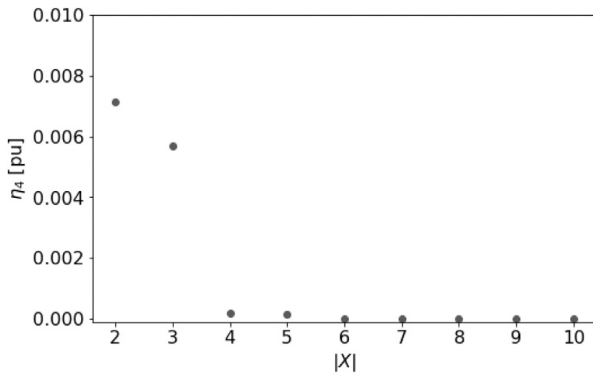**Fig. 14.** Sensitivity analysis results for η_3.

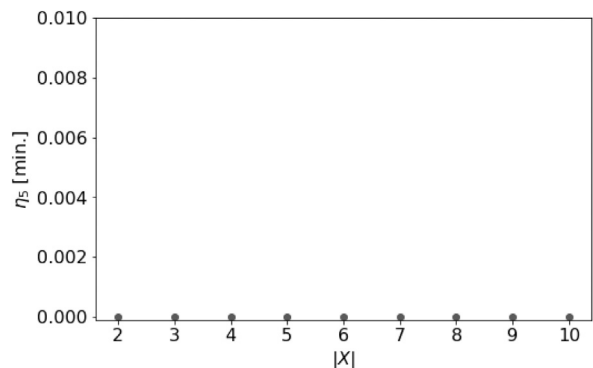**Fig. 15.** Sensitivity analysis results for η_4.

Fig. 16. Sensitivity analysis results for η_5.

could be subsequently utilized to built decentralized ANN controllers. No performance difference is observed between the proposed centralized and decentralized ANN controllers, opening the possibility for non-coordinated decentralized control with lower communication bandwidth and computational power requirements. Lastly, with the aid of SHAP, non-local grid measurements are shown to contain relevant information for decentralized ANNs to eliminate voltage problems.

For future work, we will look to implement our proposed approach in more complex ACOPF formulations such as the security-constrained ACOPF in order to test its robustness. With increasing complexity, it is expected that more complex constraint boundary tightening techniques than the one used in this paper will be needed to ensure the feasibility of ANN-derived solutions. Additionally, we aim to further test our proposed approach by building case studies based on larger grids with more nodes and higher complexity, approaching real-life grids and therefore allowing for a more accurate approximation of the benefits of our proposed approach. At the moment, such analysis would not be possible with publicly available data and hence, we hope to cooperate with electricity grid operators in the future to obtain the necessary data.

CRediT authorship contribution statement

Christian Utama: Conceptualization, Methodology, Software, Writing – original draft, Visualization. **Christian Meske:** Conceptualization, Writing – review & editing, Supervision. **Johannes Schneider:** Conceptualization, Writing – review & editing, Supervision. **Carolin Ulbrich:** Conceptualization, Writing – review & editing, Supervision.

Declaration of competing interest

The authors declare that they have no known competing financial interests or personal relationships that could have appeared to influence the work reported in this paper.

Data availability

Data will be made available on request.

References

[1] Pina A, Silva CA, Ferrão P. High-resolution modeling framework for planning electricity systems with high penetration of renewables. Appl Energy 2013;112:215–23.

[2] Thomsen J, Hussein NS, Senkpiel C, Hartmann N, Schlegl T. An optimized energy system planning and operation on distribution grid level—The decentralized market agent as a novel approach. Sustain Energy Grids Netw 2017;12:40–56.

[3] Wirth H. Recent facts about photovoltaics in Germany. Report, Fraunhofer ISE; 2021, URL https://www.ise.fraunhofer.de/en/publications/studies/recent-facts-about-pv-in-germany.html.

[4] BMWK. Erneuerbare Energien, URL https://www.bmwk.de/Redaktion/DE/Dossier/erneuerbare-energien.html.

[5] Holguin JP, Rodriguez DC, Ramos G. Reverse power flow (RPF) detection and impact on protection coordination of distribution systems. IEEE Trans Ind Appl 2020;56(3):2393–401.

[6] Fu X, Chen H, Cai R, Yang P. Optimal allocation and adaptive VAR control of PV-DG in distribution networks. Appl Energy 2015;137:173–82.

[7] Ghazvini MAF, Lipari G, Pau M, Ponci F, Monti A, Soares J, et al. Congestion management in active distribution networks through demand response implementation. Sustain Energy Grids Netw 2019;17:100185.

[8] Anaya KL, Pollitt MG. A social cost benefit analysis for the procurement of reactive power: The case of power potential. Appl Energy 2022;312:118512.

[9] Verband der Elektrotechnik, Elektronik und Informationstechnik (VDE). VDE-AR-N 4105—Technische mindestanforderungen für anschluss und parallelbetrieb von erzeugungsanlagen am niederspannungsnetz. VDE-Anwendungsregel, 2018.

[10] Verband der Elektrotechnik, Elektronik und Informationstechnik (VDE). VDE-AR-N 4110—Technische Regeln für den Anschluss von Kundenanlagen an das Mittelspannungsnetz und deren Betrieb. VDE-Anwendungsregel, 2018.

[11] Zhang Z, da Silva FF, Guo Y, Bak CL, Chen Z. Double-layer stochastic model predictive voltage control in active distribution networks with high penetration of renewables. Appl Energy 2021;302:117530.

[12] IEEE. IEEE standard for interconnection and interoperability of distributed energy resources with associated electric power systems interfaces. IEEE Std 2018;1547–2018.

[13] Zhou Y, Li Z, Wang G. Study on leveraging wind farms' robust reactive power range for uncertain power system reactive power optimization. Appl Energy 2021;298:117130.

[14] Haider R, Annaswamy AM. A hybrid architecture for volt-var control in active distribution grids. Appl Energy 2022;312:118735.

[15] Shi Y, Tuan HD, Savkin AV, Lin C-T, Zhu JG, Poor HV. Distributed model predictive control for joint coordination of demand response and optimal power flow with renewables in smart grid. Appl Energy 2021;290:116701.

[16] Sun AX, Phan DT, Ghosh S. Fully decentralized AC optimal power flow algorithms. In: 2013 IEEE power & energy society general meeting. IEEE; 2013, p. 1–5.

[17] Kargarian A, Mohammadi J, Guo J, Chakrabarti S, Barati M, Hug G, et al. Toward distributed/decentralized DC optimal power flow implementation in future electric power systems. IEEE Trans Smart Grid 2016;9(4):2574–94.

[18] Candas S, Zhang K, Hamacher T. A comparative study of benders decomposition and ADMM for decentralized optimal power flow. In: 2020 IEEE power & energy society innovative smart grid technologies conference. IEEE; 2020, p. 1–5.

[19] Hasan F, Kargarian A, Mohammadi A. A survey on applications of machine learning for optimal power flow. In: 2020 IEEE texas power and energy conference. IEEE; 2020, p. 1–6.

[20] Guha N, Wang Z, Wytock M, Majumdar A. Machine learning for AC optimal power flow. In: ICML 2019. 2019.

[21] Zamzam AS, Baker K. Learning optimal solutions for extremely fast AC optimal power flow. In: 2020 IEEE international conference on communications, control, and computing technologies for smart grids (SmartGridComm). IEEE; 2020, p. 1–6.

[22] Fioretto F, Mak TW, Van Hentenryck P. Predicting ac optimal power flows: Combining deep learning and lagrangian dual methods. In: Proceedings of the AAAI conference on artificial intelligence. Vol. 34, 2020, p. 630–7.

[23] Wang Z, Menke J-H, Schäfer F, Braun M, Scheidler A. Approximating multi-purpose AC optimal power flow with reinforcement trained artificial neural network. Energy AI 2022;7:100133.

[24] Bellizio F, Karagiannopoulos S, Aristidou P, Hug G. Optimized local control for active distribution grids using machine learning techniques. In: 2018 IEEE power & energy society general meeting. IEEE; p. 1–5.

[25] Garg A, Jalali M, Kekatos V, Gatsis N. Kernel-based learning for smart inverter control. In: 2018 IEEE global conference on signal and information processing (GlobalSIP). IEEE; p. 875–9.

[26] Karagiannopoulos S, Aristidou P, Hug G. Data-driven local control design for active distribution grids using off-line optimal power flow and machine learning techniques. IEEE Trans Smart Grid 2019;10(6):6461–71.

[27] Lundberg SM, Lee S-I. A unified approach to interpreting model predictions. In: NIPS2017. 2017.

[28] AlKaabi SS, Khadkikar V, Zeineldin H. Incorporating PV inverter control schemes for planning active distribution networks. IEEE Trans Sustain Energy 2015;6(4):1224–33.

[29] Ali A, Raisz D, Mahmoud K. Optimal oversizing of utility-owned renewable DG inverter for voltage rise prevention in MV distribution systems. Int J Electr Power Energy Syst 2019;105:500–13.

[30] Barsali S, et al. Benchmark systems for network integration of renewable and distributed energy resources. 2014.

[31] Wächter A, Biegler LT. On the implementation of an interior-point filter line-search algorithm for large-scale nonlinear programming. Math Program 2006;106(1):25–57.

[32] Thurner L, Scheidler A, Schäfer F, Menke J-H, Dollichon J, Meier F, et al. Pandapower—An open-source python tool for convenient modeling, analysis, and optimization of electric power systems. IEEE Trans Power Syst 2018;33(6):6510–21. http://dx.doi.org/10.1109/TPWRS.2018.2829021.

[33] Coffrin C, Bent R, Sundar K, Ng Y, Lubin M. Powermodels.jl: An open-source framework for exploring power flow formulations. In: 2018 power systems computation conference. 2018, p. 1–8. http://dx.doi.org/10.23919/PSCC.2018.8442948.

[34] Abadi M, Agarwal A, Barham P, Brevdo E, Chen Z, Citro C, et al. TensorFlow: Large-scale machine learning on heterogeneous systems. 2015, Software available from tensorflow.org, URL https://www.tensorflow.org/.

[35] Chollet F, et al. Keras. 2015, https://keras.io.

[36] Kingma DP, Ba J. Adam: A method for stochastic optimization. 2014, arXiv preprint arXiv:1412.6980.

[37] ENTSO-E. The transparency platform of ENTSO-E, URL https://https://www.entsoe.net/.

[38] Hofmann M, Riechelmann S, Crisosto C, Mubarak R, Seckmeyer G. Improved synthesis of global irradiance with one-minute resolution for PV system simulations. Int J Photoenergy 2014;2014.

[39] Hofmann M. Synthesized One-Minute Values for Berlin, Germany, URL https://pvmodelling.azurewebsites.net/Minutes/Get/Berlin.

[40] Dobbe R, Sondermeijer O, Fridovich-Keil D, Arnold D, Callaway D, Tomlin C. Toward distributed energy services: Decentralizing optimal power flow with machine learning. IEEE Trans Smart Grid 2019;11(2):1296–306.